Carbon 195 (2022) 154–164

Contents lists available at ScienceDirect

Carbon

journal homepage: www.elsevier.com/locate/carbon

Four-penta-graphenes: Novel two-dimensional fenestrane-based auxetic nanocarbon allotropes for nanoelectronics and optoelectronics

Mehmet Emin Kilic *, Kwang-Ryeol Lee **

Computational Science Research Center, Korea Institute of Science and Technology, Seoul, 02792, Republic of Korea

ARTICLE INFO

Article history:
Received 23 December 2021
Received in revised form
25 February 2022
Accepted 4 April 2022
Available online 7 April 2022

ABSTRACT

The great success of graphene has encouraged tremendous interest in searching for new two-dimensional (2D) carbon allotropes. Based on first-principles calculations, we proposed new 2D carbon allotropes obtained from the assembly of fenestrane molecule unit, named as four-penta-graphenes (fPG). The fPG monolayers are energetically more favorable than pentagraphene and show excellent dynamical, thermal, and mechanical stability. They exhibit exotic mechanical properties including anisotropic in-plane stiffness and auxetic behavior with sign-tunable Poisson's ratio. Their electronic properties are diverse, ranging from narrow band gap semiconductors to metal. The electronic band gap and band edge positions of the fPG semiconductors can be flexibly modulated by strain engineering. Indirect-to-direct band gap and semiconductor-to-metal transitions can be achieved by applying compressive and tensile strains, respectively. High mobility and anisotropic effective mass of carriers make these materials promising for nanoelectronics. Using many-body GW_0+BSE approximations, we reveal that the fPG semiconductors exhibit strong excitonic effects with distinct optical absorption peaks in the visible range. These remarkable optical properties make them also promising devices for optoelectronics.

1. Introduction

Carbon is a chemically unique element that can adopt different hybridization states such as *sp*, sp^2, and sp^3, allowing diverse covalent bonding between carbon atoms and thereby producing a wide variety of allotropic forms having different properties. The two natural allotropes of carbon, graphite and diamond, composed entirely of sp^2- and sp^3-hybridized carbon atoms, respectively, exhibit strikingly opposite properties. For instance, diamond is superhard and insulator whereas graphite is ductile, ultrasoft, and conductor. The discovery of graphene, which is a single layer of graphite, has become one of the most exciting topics of research due to its intriguing properties, such as high stiffness, high carrier mobility, and room temperature quantum Hall effects. These exceptional properties enable graphene to be used in various applications such as nanoelectronics, fuel cells, and energy storage devices [1–4].

In recent years, lots of researchers have striven to move beyond graphene. A large family of 2D graphene allotropes containing a mixture of *sp*-, sp^2-, and sp^3-hybridized carbon atoms has been reported theoretically and experimentally [5–7]. Some of them show superior material properties that can outperform graphene. For instance, graphyne has unique *sp*-sp^2-hybridized carbon atoms, known as natural uniform nanopores and highly π-conjugated structure, which endow it great potential in applications such as gas separation and catalysis [8]. Moreover, phagraphene, a low-energy graphene allotrope, exhibits direction-dependent distorted Dirac cones, which is **appealing for nanoelectronics** [9].

Inspired by the synthesis of pure pentagon-based C_{20} cage [10], we witness a continuously growing research in pentagonal units going beyond conventional hexagonal and tetragonal units. For instance, silicon nanoribbons comprising pentagonal rings have been grown on Ag (100) [11]. In parallel with these advancements, atomically thin pentagonal $PdSe_2$ crystal exfoliated from bulk structure has been experimentally revealed [12] and show a high air stable behavior with highly anisotropic optical, electrical, and optoelectronic properties [13]. Zhang *et al.* theoretically predicted a 2D pentagonal monolayer, pentagraphene (PG), containing a mixture of sp^2-sp^3 -hybridized carbons, and possessing unusual negative Poisson's ratio and ultrahigh ideal strength [14]. The

* Corresponding author.
** Corresponding author.
E-mail addresses: mekilic@kist.re.kr (M.E. Kilic), krlee@kist.re.kr (K.-R. Lee).

https://doi.org/10.1016/j.carbon.2022.04.018
0008-6223/

unique properties of 2D pentagonal materials make them attractive for energy-related applications. For instance, metallic penta-BN_2 with excellent electrical conductivity is suggested to be promising for Li-ion battery anodes [15]. In our previous study, we have proposed group-IV penta-carbides as promising 2D semiconducting materials for photocatalytic water splitting [16]. By applying Stone-Wales transformation to the penta-carbides, tetra-hex-carbides with exceptional electronic properties, such as sizable direct band gap and anisotropic high carrier mobility, have been proposed to be promising for nanoelectronics [17]. Silva *et al.* proposed a new family of carbon allotropes, namely tripentaphenes [18]. These allotropes are composed of three contiguous pentagons and exhibit metallic behavior with different Dirac cones, making them promising for nanoelectronics. Very recently, Me-graphene [19] and C568 [20], which are apparently the same structures (visible in their supercells) and composed entirely of four-penta (fP) units, have been proposed to be a transition structure between graphene and PG.

In this paper, inspired by the [5.5.5.5.]Fenestrane [21] molecule consisting of four contiguous pentagons (or fP unit), we reported our prediction of newly PGallotropes, namely "four-penta-graphene" abbreviated as fPG. Using first-principles calculations, we systematically studied the stability and intrinsic properties of three forms of the fPG allotropes, namely α-fPG, β-fPG, and γ-fPG. At first, we investigated the stability of the fPG monolayers from the energetic, dynamical, thermal, and mechanical aspects based on the formation energy, phonon band dispersion, *ab-initio* molecular dynamics (AIMD), and elastic tensor analysis, respectively. We further examined their mechanical, electronic, transport, and optical properties, and compared them with PG. It should be noted that the α-fPG monolayer is the same structure of Me-graphene or C568 monolayer. We hope that the unique properties of the fPG monolayers will enrich the family of 2D pentagonal materials.

2. Computational methods

All first principle calculations were performed using Vienna *ab-initio* simulation package (VASP) [22] on density functional theory (DFT). To describe the electron-ion interaction, the projector-augmented wave (PAW) approach [23] was used. The exchange-correlation contributions for the structural optimization and electronic structure calculations were treated using the generalized gradient approximation (GGA) with Perdew-Burke-Ernzerhof (PBE) [24]. In particular, considering the underestimated electronic band gap in PBE, electronic band structures were also calculated by the Heyd–Scuseria–Ernzerhos hybrid functional (HSE06) [25] constructed by mixing 0.25 of the nonlocal Fock exchange with 0.75 of PBE exchange and screening length of $\lambda = 0.2$ Å^{-1} and GW approximation [26]. The structure optimizations were carried out using a conjugate gradient algorithm until the residual forces on atoms reach values smaller than 0.01 eV Å^{-1} as well as a stress tensor tolerance of 0.1 GPa. Electronic wave functions were expanded in a plane-wave basis set, with an energy cutoff of 520 eV. To avoid the periodic interaction, a vacuum thickness of 20 Å was added in the vertical direction. The Brillouin zone (BZ) was sampled with *k*-meshes of $32 \times 32 \times 1$, $24 \times 24 \times 1$, $18 \times 24 \times 1$, and $18 \times 18 \times 1$ were carefully tested for PG, α-fPG, β-fPG, γ-fPG monolayers, respectively. Phonon band dispersions were calculated by using the PHONOPY code [27] based on a supercell approach. To test the thermal stability of the examined structures, we performed AIMD simulations at a constant temperature ensemble (NVT) using Nose thermostat [28] of which the time step is 1 fs. We used $5 \times 5 \times 1$, $3 \times 3 \times 1$, $3 \times 4 \times 1$, and $3 \times 3 \times 1$ supercells for PG, α-fPG, β-fPG, and γ-fPG monolayers, respectively, enabling to reduce the constraints arising from periodic boundary condition and to detect the possible structure reformation at elevated temperatures.

The two mechanical constants, including Young's modulus (Y^{2D}) and Poisson's ratio ($\nu(\theta)$) as a function of the in-plane angle θ were calculated in the following expressions [29],

$$Y^{2D}(\theta) = \frac{C_{11}C_{22} - C_{12}^2}{C_{11}s^4 + C_{22}c^4 + \left(\frac{(C_{11}C_{22}-C_{12}^2)}{C_{66}} - 2C_{12}\right)s^2c^2} \quad (1)$$

$$\nu(\theta) = \frac{C_{12}(s^4 + c^4) - \left(C_{11} + C_{22} - \frac{(C_{11}C_{22}-C_{12}^2)}{C_{66}}\right)s^2c^2}{C_{11}s^4 + C_{22}c^4 + \left(\frac{(C_{11}C_{22}-C_{12}^2)}{C_{66}} - 2C_{12}\right)s^2c^2} \quad (2)$$

where $s = \sin(\theta)$ and $c = \cos(\theta)$.

3. Results and discussion

3.1. Structure characterization

The fully relaxed atomic structure of the fPG monolayers is presented in Fig. 1. From the view of the formation mechanism, α-fPG having the space group of *P*-4*m*2 (no. 115), can be constructed by the direct connection of the fP units along the **a** and **b** lattice directions. Similar to PG, α-fPG is composed of sp^2- and sp^3-hybridized carbon atoms, but with different ratios. Such that, the sp^3 to sp^2 ratio in α-fPG monolayer is one to twelve while that in PG is two to four. Besides, the sp^3 carbon atom density in α-fPG (0.03 atom/Å^2) is much lower than that in PG (0.15 atom/Å^2). For β-fPG, the structure belongs to *P*-*mm*2 symmetry (no. 25), and can be formed by the connection of the fP units where they are directly linked along the **b** lattice direction while are linked by acetylenic linkages along the **a** lattice direction. The existence of acetylenic linkages makes β-fPG to be a low-density and light 2D carbon allotrope with respect to PG and α-fPG. Such that, the atom density in β-fPG is 0.35 atom/Å^2 is lower than that in PG (0.45 atom/Å^2), α-fPG (0.39 atom/Å^2), and graphene (0.38 atom/Å^2). As for γ-fPG, the fP units are connected by acetylenic linkages along the **a** and **b** lattice directions to form the crystal structure. The structure belongs to space group of *P*-4*m*2 (no. 115). The unitcell of β-fPG and γ-fPG is composed of sp-sp^2-sp^3 hybridized carbons where the ratio of sp: sp^2: sp^3 is about 4:12:1 and 8:12:1, respectively. For convenience of discussion, we hereafter group the sp, sp^2, and sp^3-hybridized carbons as C_1, C_2, and C_3 respectively. As there exists different hybridized carbons in the fPG monolayers, resulting in different bond character, we define d_{11}, d_{12}, d_{22}, and d_{23} for the bond length of C_1–C_1, C_1–C_2, C_2–C_2, and C_2–C_3, respectively. The optimized lattice constants (a and b), the corresponding bond lengths (d_{ij}), and thickness (h) of PG and the fPG monolayers are summarized in Table 1. We found that the C_1–C_1 bond length of $d_{11} = 1.23$ Å in β-fPG and γ-fPG is almost the same that in graphyne (1.20 Å) [33], showing their triple bond character. Likewise, the sp-sp^2 bond length for β-fPG (γ-fPG) about 1.37 Å (1.38 Å) is close to that in graphyne (about 1.40 Å) [33]. For sp^2-sp^2 bond length, all the fPG monolayers have $d_{22} = 1.43$ Å, which is relatively higher than that in PG (1.34 Å) [14], but is close to that in graphene (1.42 Å). As for sp^2-sp^3 bond length, the d_{23} of 1.56 Å, 1.58 Å, and 1.57 Å for α-fPG, β-fPG, and γ-fPG, respectively, is slightly lower than that of PG (1.57 Å) [14].

3.1.1. Structure stability

To examine the energetic stability of the fPG monolayers, we performed the total energy calculations. As presented in Fig. 2 (a), α-fPG with a total energy of −8.83 eV is energetically more

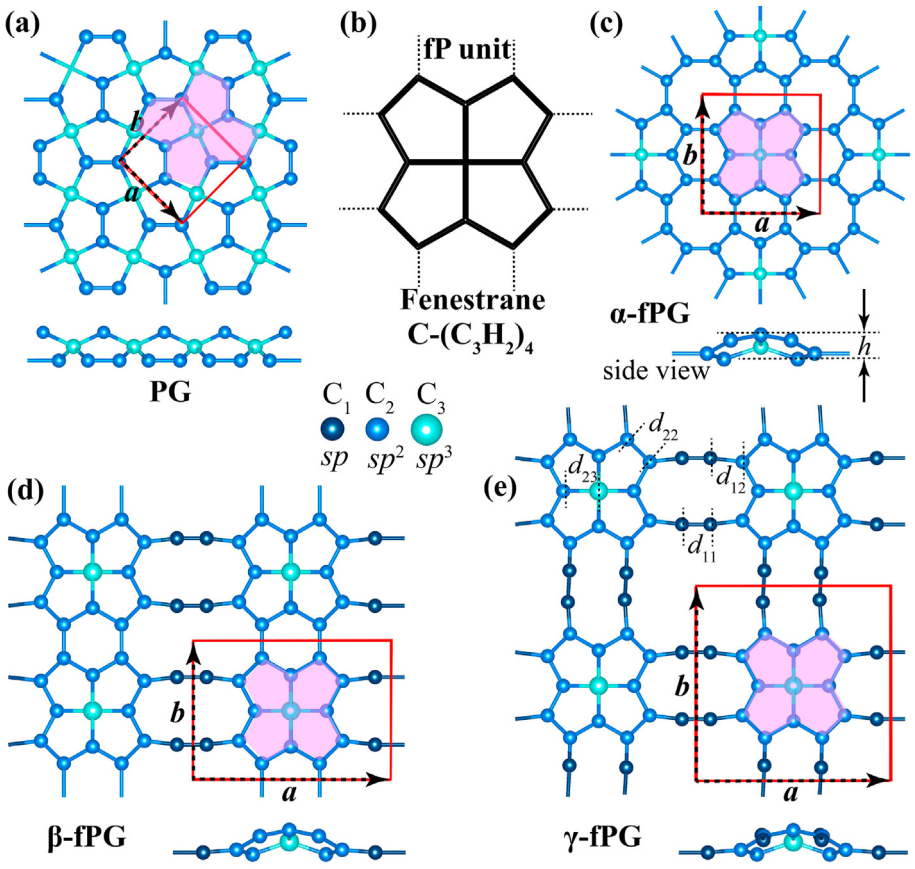

Fig. 1. Optimized atomic structure of (a) PG, (b) molecular unit of fenestrane molecule (four penta unit, fP), (c) α-fPG, (d) β-fPG, and (e) γ-fPG monolayers. Three inequivalent carbon atoms labeled as $C_1(sp)$, $C_2(sp^2)$, and $C_3(sp^3)$ are denoted different colors as depicted inset. The red line represents the unitcell where the lattice vectors, **a** and **b**, are marked with dashed black arrows. The buckling height (h) and bond lengths (d_{ij}) are depicted. The fP units are shaded by pink color. (A colour version of this figure can be viewed online.)

favorable than other sp^2-sp^3 hybridized carbon allotropes including tetrahexcarbon (−8.36 eV per C) and PG (−8.32 eV per C). Likewise, β-fPG and γ-fPG with the total energy of −8.62 eV per C and −8.51 eV per C, respectively, are also energetically favorable compared with other 2D carbon allotropes including sp-hybridized carbons such as experimentally synthesized graphdiyne allotropes [6] (see Fig. 2 (b)). To examine the synthesizability of the fPG monolayers, we calculated the formation energy difference (ΔE) between the fPG monolayers and graphite as a reference bulk, and compared with the other theoretically predicted and experimentally realized 2D carbon allotropes. The ΔE of 398, 607, and 711 meV per C atom for α-fPG, β-fPG, and γ-fPG respectively, is lower than that for the experimentally synthesized γ-GDY (about 823 meV per C atom) [6]. Thus, the low ΔE infers the easy fabrication of the fPG monolayers from the corresponding reference bulk structure, suggesting that the predicted 2D carbon allotropes can exist in reality.

To check the dynamic stability of the fPG monolayers, we performed the lattice dynamics phonon calculations, providing the phonon dispersion curves and atom-projected phonon density-of-states (PhDOS). It is clear from Fig. 3 (a) that the fPG monolayers are free from any imaginary frequencies in the whole BZ, confirming their dynamic stability. Similar to PG, the highest phonon frequency in α-fPG mainly comes from the vibration of the sp^2-hybridized carbon atoms (C_2). The phonon spectrum of β-fPG and γ-fPG has a distinct phonon gap ranging from ~1550 cm^{-1} to ~2120 cm^{-1}. We observed that the highest phonon frequencies, having relatively dispersionless phonon branches, are originated from the vibration of sp-hybridized carbon atoms. The unsymmetrical stretching vibration of central C≡C bonds in β-fPG and γ-fPG emerges a phononic gap in the phonon spectrum. The highest phonon frequency of PG, α-fPG, β-fPG, and γ-fPG monolayers is found to be 1632, 1578, 2187, and 2197 cm^{-1}, respectively. This suggests the strong bond network in the fPG monolayers.

Next, we investigated the thermal stability of the fPG monolayers by performing AIMD simulations. We first heated the supercell structures at 300 K for 10 ps. After ensuring thermal equilibrium at that temperature, the monolayers were gradually heated to 900 K and 1200 K for 10 ps (Figure S1 of Supporting Information (SI)). As the potential energy is sensitive to bond breaking and atom re-arrangements, we monitored the energy change during the AIMD simulations. We observed that the energy is almost constant with very small fluctuations resulting from the thermal oscillations of atoms around their equilibrium positions. Moreover, the snapshot of atomic configurations of PG and the fPG monolayers at the end of the AIMD simulations at various temperatures is displayed in Fig. 3 (b). Such results indicate that the

Table 1
Optimized lattice constants a and b, buckling thickness h, bond length d_{11}, d_{12}, d_{22}, and d_{23} in Å, electronic band gap obtained from the PBE and HSE06 functionals, and band gap energy type for PG, α-fPG, β-fPG, γ-fPG monolayers.

	a	b	h	d_{11}	d_{12}	d_{22}	d_{23}	E_g^{PBE}	E_g^{HSE}	Type
PG	3.64	3.64	1.21	–	–	1.34	1.55	2.38	3.26	Indirect
α-fPG	5.75	5.75	0.98	–	–	1.43	1.56	0.64	1.06	Indirect
β-fPG	8.27	5.79	0.99	1.23	1.37	1.43	1.58	0.20	0.43	Indirect
γ-fPG	8.25	8.25	1.06	1.23	1.38	1.43	1.57	–	–	Metallic

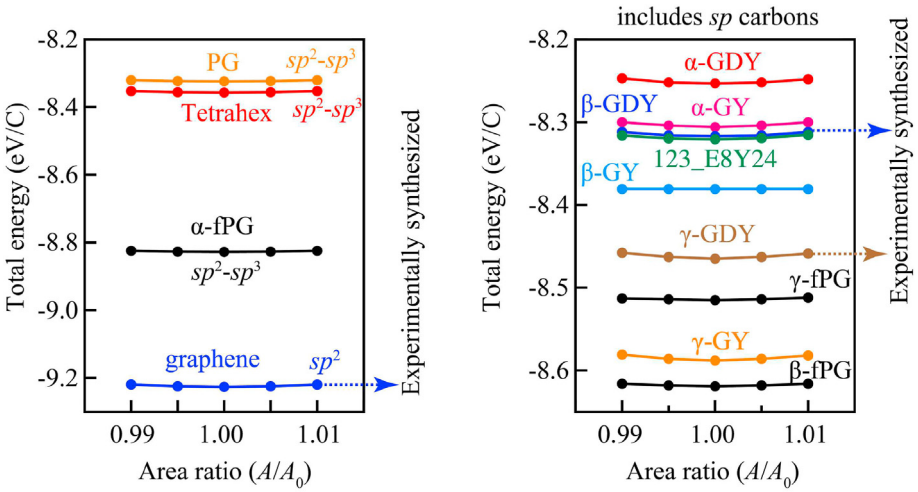

Fig. 2. Variation of total energy with respect to area ratio for α-fPG, β-fPG, γ-fPG monolayers and their comparison with other 2D carbon allotropes, including graphene, PG, tetrahexcarbon, 123_E8Y24 [30], α-, β-, γ-graphyne (GY) [31] and their graphdiyne (GDY) [32] counterparts. (A colour version of this figure can be viewed online.)

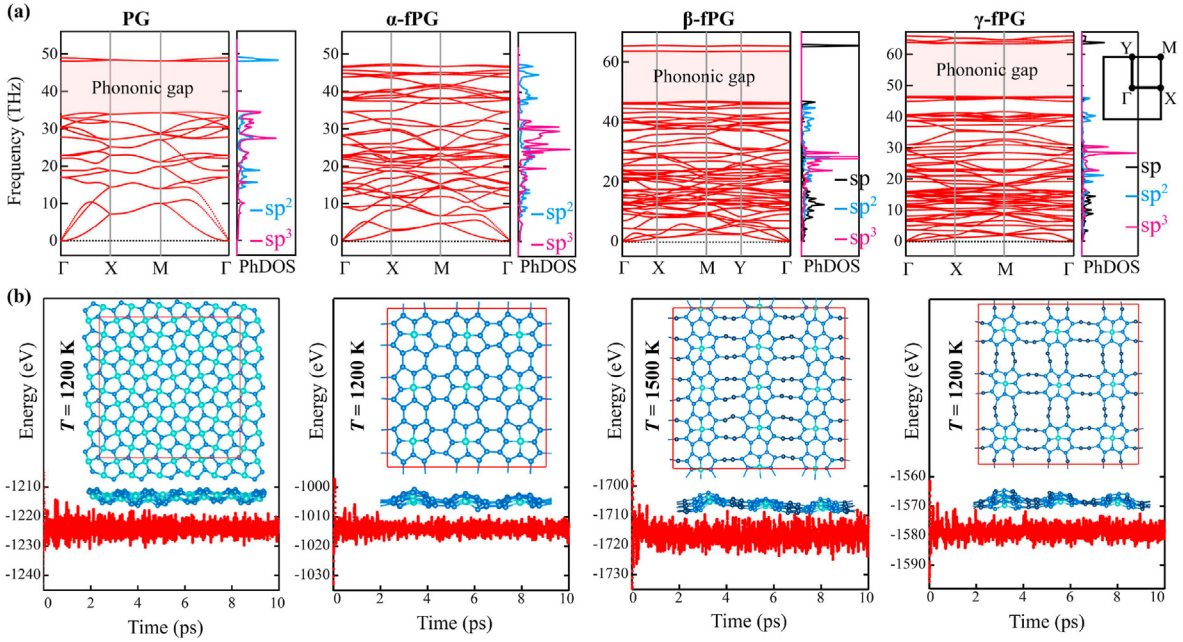

Fig. 3. (a) Phonon band dispersion with atom-projected phonon density of states (PhDOS) and (b) variation of potential energy for 10 ps at high temperature (1200–1500 K) for PG, α-fPG, β-fPG, and γ-fPG. Inset shows the atomic configurations at the end of the AIMD simulations. (A colour version of this figure can be viewed online.)

monolayers can survive at high temperatures, determining their suitability for technological applications above room temperature.

To further examine the ability to withstand small mechanical deformation, we studied the mechanical stability of the fPG monolayers by evaluating the well-known Born-Huang elastic stability criteria [34] as $C_{11}C_{22} - C_{12}^2 > 0$ and $C_{66} > 0$ where C_{ij} are in-plane elastic constants obtained from the energy-strain relations. The strain energy per unit area (U_s) is defined as,

$$U_s(\epsilon) = \frac{1}{2}C_{11}\epsilon_{xx}^2 + \frac{1}{2}C_{22}\epsilon_{yy}^2 + C_{12}\epsilon_{xx}\epsilon_{yy} + 2C_{66}\epsilon_{xy}^2 \quad (3)$$

where ϵ_{ij} are the corresponding in-plane strains and defined as $\epsilon_{ij} = (l - l_0)/l_0$, where l_0 and l are the equilibrium and strained lattice values, respectively. We applied various in-plane mechanical deformations including uniaxial, biaxial, and shear strains in the range of −2 to 2% with an increment of 0.5%, and calculated the strain energy at each strain. The strain energy *vs* strain for the fPG monolayers is plotted in Figure S2 of SI where the second derivative presents the corresponding elastic constants according to Eq. 3. The

Table 2
Calculated elastic constants (C_{ij}) in N/m, Young's modulus (Y^{2D}) in N/m, and Poisson's ratios (ν) of PG, α-, β-, and γ-fPG monolayers.

	C_{11}	C_{22}	C_{12}	C_{66}	Y_a^{2D}	Y_b^{2D}	ν_a	ν_b
PG	267.5	267.5	−18.8	151.0	266.2	266.2	−0.070	−0.070
α-fPG	209.9	209.9	0.7	102.4	209.9	209.9	0.004	0.004
β-fPG	181.2	160.8	−0.9	19.4	181.2	160.8	−0.005	−0.005
γ-fPG	115.7	115.7	−8.5	7.9	115.1	115.1	−0.073	−0.073

obtained elastic constants of the fPG monolayers are listed in Table 2. The results reveal that the elastic constants of the fPG monolayers meet the Born stability criteria, confirming their mechanical stability.

3.2. Mechanical properties

After revealing the robust stability of the fPG monolayers, we investigated their intrinsic mechanical properties by calculating two independent mechanical constants as Young's modulus (Y^{2D}) and Poisson's ratio (ν) with different in-plane crystal orientations using Eq. 1 and Eq. 2, respectively. It is evident from Fig. 4 (a) that, similar to PG, the Y^{2D} of α-fPG is rather isotropic in the in-plane of the sheet. The change of Y^{2D} with respect to θ (which is relative to the positive x-axis in the unitcell) in α-fPG is about 1%, confirming the isotropic mechanical response. The largest Y^{2D} value of 209.9 N/m for α-fPG is found along the **a** lattice direction (0°). This value is relatively lower than that of other sp^2–sp^3-hybridized carbon allotropes, including PG (267.5 N/m) [14,16] and tetrahexcarbon (286.12 N/m) [35]. Moreover, the Y^{2D} shares the minimum value of 207.7 N/m in the diagonal direction (45°). Contrary to α-fPG, β-fPG and γ-fPG exhibit strong anisotropic Young's modulus. From α-fPG to β-fPG, the Y^{2D} reduces due to the presence of acetylenic linkages. The maximum Y^{2D} value of 181.2 N/m in β-fPG monolayer can be obtained along the **a** lattice direction ($\theta = 0°$), which is higher than that of other carbon allotropes containing acetylene linkages such as graphyne (127 ~137 N/m) and graphdiyne (104 ~118 N/m) [36]. With the increase of θ angle from 0° to 90°, the Y^{2D} first rapidly decreases to 63.1 N/m at $\theta = 45°$, and then increases where the Y^{2D} value approaches to 160.8 N/m for $\theta = 90°$. Likewise, the Y^{2D} in γ-fPG reduces because of the existence of the extra acetylenic linkages. The maximum Y^{2D} value is calculated as 115.7 N/m in the **a** lattice direction ($\theta = 0°$) while the minimum value is about 27.5 N/m in the diagonal direction ($\theta = 45°$). Thus, the results imply that β-fPG and γ-fPG are relatively much stiffer along the lattice directions (**a** or **b**) than along the diagonal direction ($\theta = 45°$) where they exhibit mechanical flexibility. That is, the apparently low Young's modulus of β-fPG and γ-fPG along the diagonal direction enables them to be easily stretchable and soft along this direction.

As for Poisson's ratio (PR), PG exhibits auxetic behavior with near zero negative PR (about −0.07) while α-fPG has zero PR (0.00). The results of the direction-dependent PR, illustrated in Fig. 4 (b), reveal that α-fPG exhibits a rather isotropic mechanical response in the plane. For β-fPG and γ-fPG, similar to PG, both exhibit an auxetic behavior with a near zero negative PR in the a and b lattice directions. However, both have positive PR in other spatial directions. Unlike α-fPG, β-fPG and γ-fPG display a highly anisotropic mechanical response. In general, the fPG monolayers have the near zero PR in the lattice directions, indicating that they do not transversely deform in response to an axial applied strain. As Poisson's ratio of 2D materials is sensitive to strain [37], we further evaluated PR of the fPG monolayers for a large strain regime. We plotted the variation of the transverse strain to longitudinal axial strain ranging from −4 to 10% in Fig. 5. It can be seen that the transverse strain for α-fPG monotonically decreases with the tensile strain. Thus, the monolayer exhibits a positive PR under uniaxial tensile strain. With enhancing compressive strain, on the other hand, the transverse strain also decreases, indicating the emergence of an auxetic behavior (negative PR). We thus reveal that α-fPG exhibits auxetic behavior under uniaxial compressive strain whereas it is a non-auxetic monolayer under uniaxial tensile strain (Fig. 5 (a)). For β- and γ-fPG, with the tensile strain, the transverse strain decreases until the PR reaches to zero and then a positive PR takes place at ~2% and ~5%, respectively (Fig. 5(b) and (c)). That is, the auxetic mechanical response in β-fPG and γ-fPG disappeared beyond these strain points. Consequently, we show that the sign of PR in the fPG monolayers can be easily tuned by strain engineering.

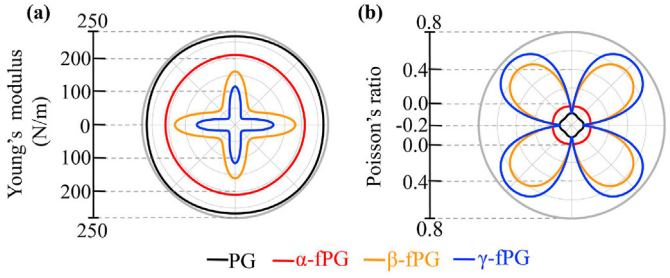

Fig. 4. Polar diagram for (a) Young's modulus in the unit of N/m and (b) Poisson's ratio of PG, and the fPG monolayers. (A colour version of this figure can be viewed online.)

To uncover the underlying mechanism of the near zero PR with sign-tunable nature in the fPG monolayers, we studied the evolution of structural parameters including bond lengths and bond angles under uniaxial deformations. The variation of bond lengths, bond angles, and bond projections for the β-fPG monolayer during the uniaxial strains along the x and y directions are presented in Figure S3 of SI. It can be seen that with enhancing the strain along the x direction, C_2–C_3 bond length lying on the yz-plane decreases, corresponding a positive PR. However, its projection in the y-direction increases up to a threshold value of 2–3% strain (corresponding to a negative PR), and then subsequently decreases with further strains (corresponding to a positive PR). Thus, the sign-tunable PR nature seems to be a consequence of the change of C_2–C_3 bonds. For C_2–C_2 bonds, we consider four types of bonds, denoted as d_{2a}, d_{2b}, d_{2c}, and d_{2d} in the fP units. We observed that d_{2a} bond lying on y-axis slightly increases with enhancing strain, corresponding a negative PR. The d_{2c} and d_{2d} bonds increase with the increase of strain while the bond angles α_3 and α_4 decrease. The d_{2b} bond increases with increasing x direction strain up to 3% while the bond angle α_1 decreases, and then, with further strains both subsequently turn to opposite directions. The change of the projection of C_2–C_2 bonds in the y direction is relatively small, resulting in a near zero PR with negative and positive values. Consequently, the sp^2 and sp^3 carbon atoms combined together act as the primary factor for emerging a near zero PR with sign-tunable nature in the fPG monolayer. Similar behavior is also observed with enhancing the strain along the y direction.

3.3. Electronic properties

As the physical properties of carbon allotropes having different hybridization states are quite different, it is of great interest to examine the electronic properties of the fPG monolayers. By adopting the PBE and HSE06 functionals, we calculated the electronic band structures and extracted the band gap energies, summarized in Table 1. Fig. 6 shows the electronic band structure with projected density-of-states (pDOS) of the fPG monolayers at the HSE06 method. Our results reveal that α-fPG and β-fPG are natural semiconductors while γ-fPG shows metallic character. As a benchmark, we calculated the electronic band gap of PG about 3.26 eV, agreeing well with previous theoretical result [14]. Although PG and α-fPG are composed of the same type hybridized carbons (sp^2-sp^3), the band gap energy in α-fPG is significantly reduced to be 1.06 eV. The decrease in the band gap energy can be explained by the ratio of sp^3 to sp^2 carbons, which is 2–4 for PG and 1 to 12 for α-fPG. In our previous study, we clearly showed that the band gap energy in sp^2-sp^3 hybridized carbon allotrope is significantly increased by changing the sp^2-hybridized carbons to sp^3 as

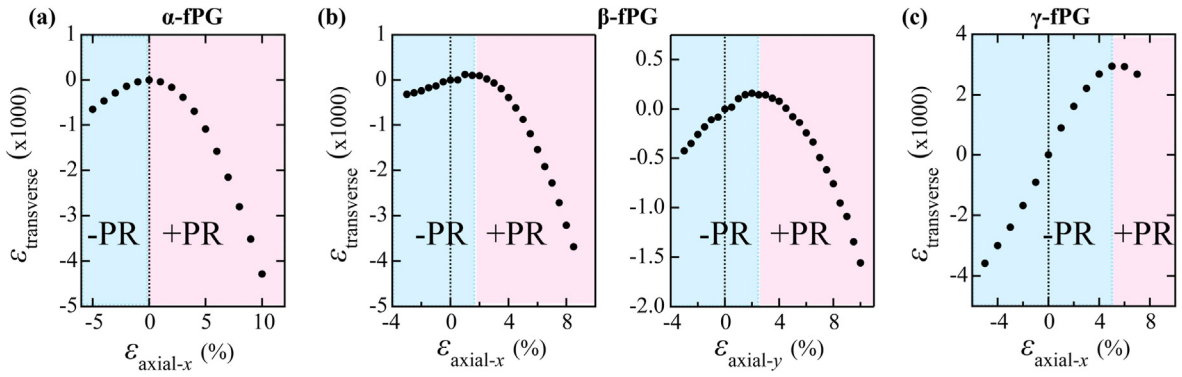

Fig. 5. Variation of transverse strain with respect to applied axial strain for (a) α-fPG (b) β-fPG, and (c) γ-fPG. The blue and pink shaded areas represent negative and positive Poisson's ratio, respectively. (A colour version of this figure can be viewed online.)

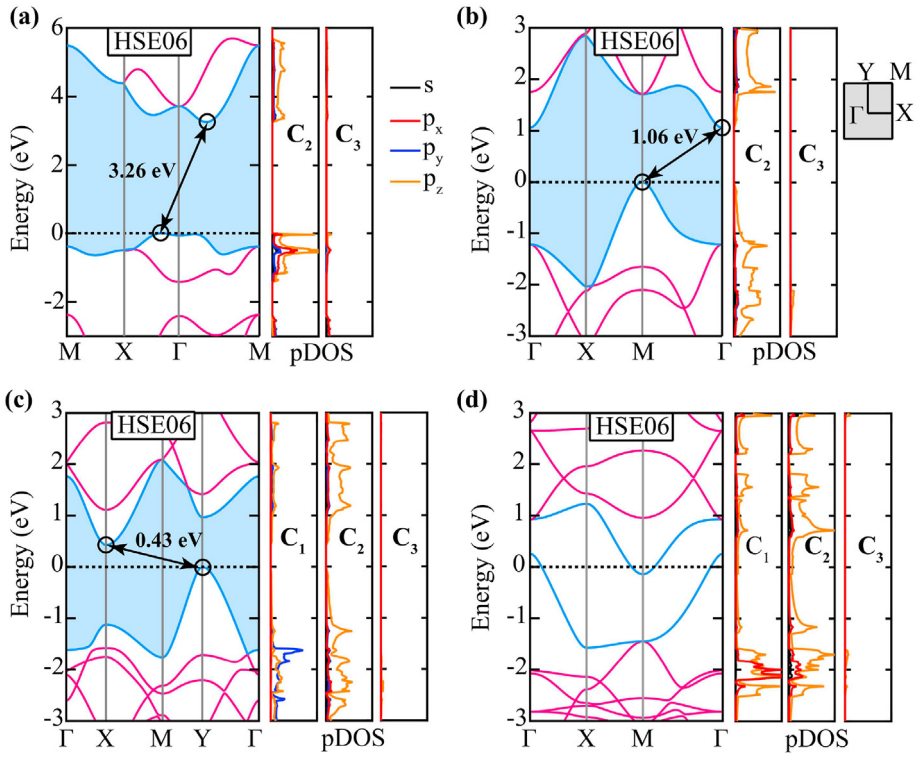

Fig. 6. Obtained the HSE06 level electronic band structure with atom- and orbital-projected density-of-states (pDOS) of (a) PG, (b) α-fPG, (c) β-fPG, and (d) γ-fPG. The VBM and CBM in electronic band structure are depicted by blue. The VBM is shifted to the Fermi energy level which is set to 0 eV, and shown with black dashed line. The electronic band gap is illustrated by black arrow. (A colour version of this figure can be viewed online.)

the sp^3-hybridization can localize the electronic states to the fragment delocalized π bond to open the band gap [35,38]. Hence, the results highlight the principal role of the sp^2/sp^3 ratio in the electronic properties of the fPG monolayers. As for sp-sp^2-sp^3 allotropes, β-fPG has the band gap energy of 0.42 eV while γ-fPG is metallic due to the crossing of two bands at the Fermi level. We found that the insertion of acetylenic groups in between fP units results in reducing the band gap energy. According to the pDOS, the main states around the Fermi level are contributed by C_2-p_z orbitals rather than C_1 and C_3 atoms.

3.3.1. Band gap tuning by strain engineering

2D materials are well-suitable for strain engineering because of their ultra-high flexibility. The emergence of exotic electronic properties such as the tunable band gap energy and band gap transition by strain engineering, which has been shown in recent studies [17,39], motivated us to examine the electronic properties of the fPG semiconductors (α-fPG and β-fPG) under strain. As the band edge positions and band gap energy are two crucial parameters for nanoelectronics and optoelectronics, we studied their variations by strain engineering and presented in Fig. 7 and Figure S4 of SI. The results revealed that the energy level of VBM and CBM for α-fPG and β-fPG subjected to strain decreases with tension and increases with compression. This indicates that the kinetic energy of the state is proportional to the reciprocal lattice vector, which decreases with the increase of lattice parameters. We also noticed that the change in the VBM energy is comparatively smoother than that in the CBM with the applied strain, resulting in the band gap energy reduction. Remarkably, the strain changes not only the energy of the band edges but also their positions in

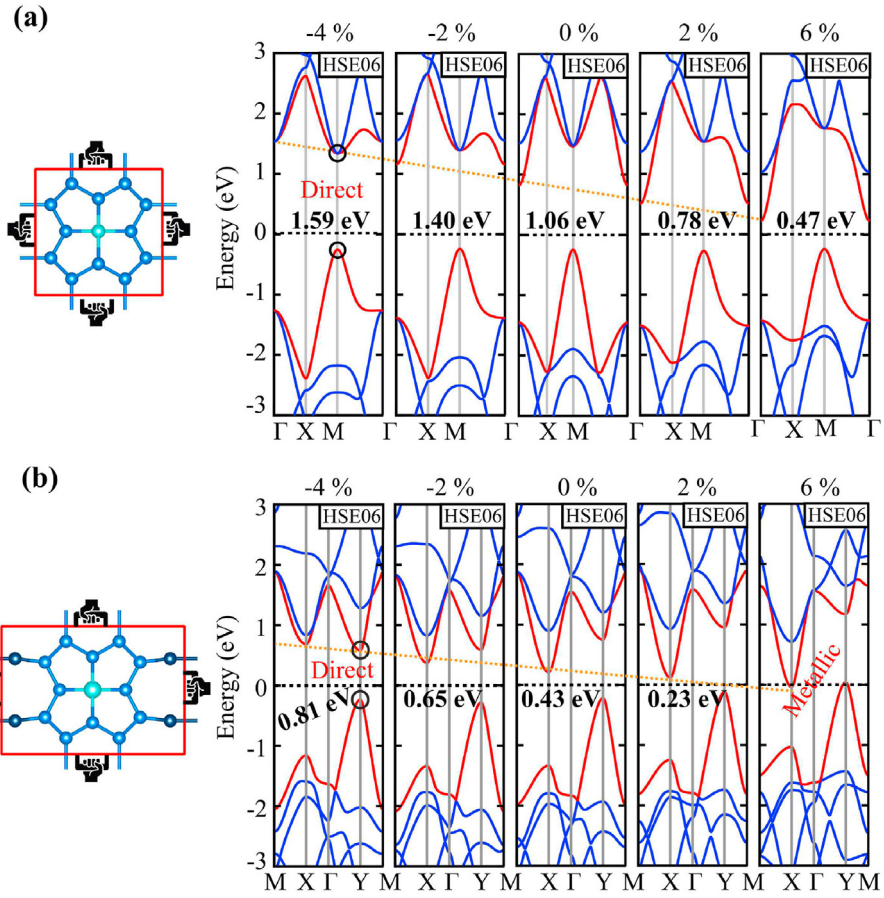

Fig. 7. Obtained the HSE06 level electronic band structures of (a) α-fPG and (b) β-fPG subjected to equi-biaxial strains ranging from −4 to 6%. The VBM and CBM bands are depicted by red color. The Fermi energy is set to 0 eV. (A colour version of this figure can be viewed online.)

momentum space. As shown in Fig. 7, at −4% equi-biaxial strain, the position of CBM is shifted from Γ to M in α-fPG and from X to Y in β-fPG. Thus, both α-fPG and β-fPG present an intriguing indirect-to-direct band gap transition at this strain where the direct band gap energy is about 1.59 eV and 0.81 eV, respectively. On the other hand, the tensile strain can result in a semiconductor−to-metal transition. In this respect, the change of the geometric structure by strain leads to the change in the energy level of band edges as well as the band gap energy, and consequently, alters the electronic properties of the monolayers. The electronic band structures under uniaxial strain are also presented in Figure S5 and S6 of SI. As a consequence, our first-principle calculations revealed that the band gap and band edge positions of the fPG monolayers can be effectively tailored by strain engineering.

3.3.2. Anisotropic effective mass and high carrier mobility

We further evaluated the potential applications of the fPG monolayers in nanoelectronics. As γ-fPG monolayer is metallic, we only analyzed the effective mass and carrier mobility for α-fPG and β-fPG semiconductors. The carrier effective mass (m^*) is obtained from the fitting data near band edges (VBM and CBM) with quadratic polynomial using $m^* = \hbar[\partial^2 E(k)/\partial k^2]^{-1}$ where k is the wave-vector and $E(k)$ is the electronic band dispersion obtained from the HSE06 method. As illustrated in Fig. 8 (a) and (c), the parabolic fittings of the band edges along the x and y directions fit well with the calculations. For α-fPG, the calculated effective mass of electron in the x (or y) direction (Γ-X (or Y) direction) is 0.17 m_0 while the hole effective mass in the same direction (M-X (or Y) direction) is about 0.16 m_0 where m_0 is the free electron effective mass. Such a low effective mass of carriers is expected to be associated with a high carrier mobility.

For β-fPG, the electron effective mass in the x and y directions is found to be 0.23 m_0 and 0.31 m_0, respectively, which are relatively higher than that of α-fPG. Moreover, the hole effective mass in the x and y directions is about 0.14 m_0 and 0.19 m_0, respectively. Thus, the effective mass of charge carriers in β-fPG exhibits an anisotropic behavior. Being able to gain a visual understanding of the anisotropy in β-fPG, we next calculated the effective mass of charge carriers from Γ to A arbitrary directions, and illustrated in Fig. 9. It can be seen that the effective mass of both hole and electron displays an approximate “8” shape, verifying the strong anisotropic transport behavior. Moreover, we examined the direction-dependent effective mass of the charge carrier when β-fPG is subjected to an in-plane isotropic strain. As depicted in Fig. 9, the anisotropy in the effective mass of electrons and holes of β-fPG is improved by strain engineering.

Next, we calculated the carrier mobility (μ) in the framework of deformation potential (DP) theory on the basis of effective mass approach proposed by Bardeen and Shockley [40] in the following equation,

$$\mu_i = \frac{e\hbar^3 C_i}{k_B T m_i^* m_d E_{d,i}^2} \tag{4}$$

where $m_d = \sqrt{m_x^* m_y^*}$ is the average effective mass. $E_{d,i}$ is the DP

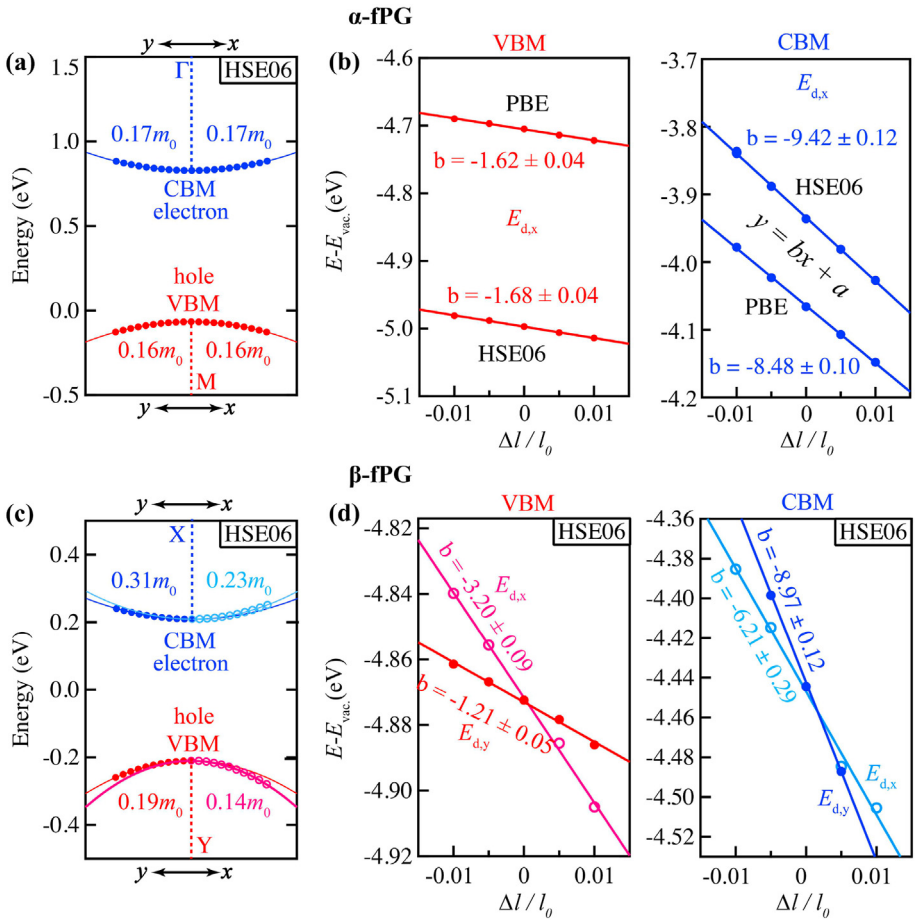

Fig. 8. Curvature of the energy (obtained from the HSE06 functional) with respect to k in the proximity of the band edges along x and y directions for (a) α-fPG and (c) β-fPG. Variation of the band edge energies with respect to very small uniaxial strain ranging from −1 to 1% for deformation potentials constants of (b) α-fPG and (d) β-fPG. (A colour version of this figure can be viewed online.)

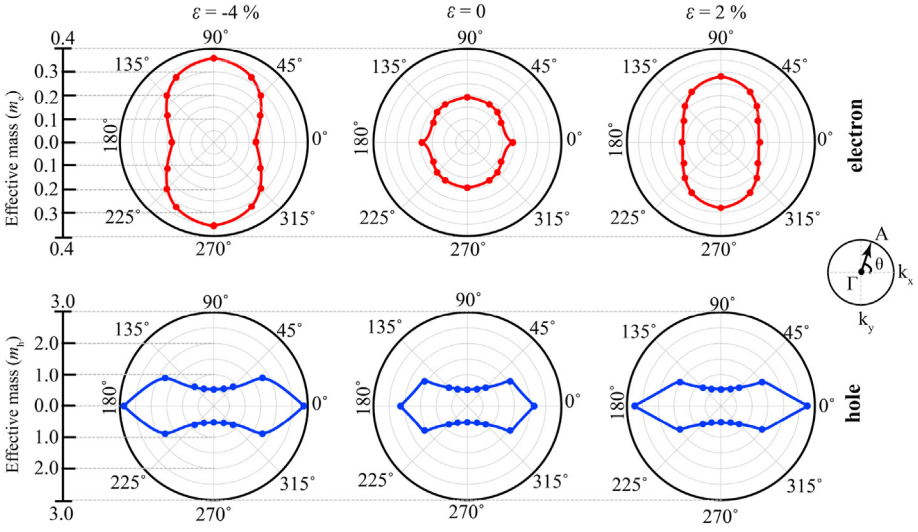

Fig. 9. Direction-dependent effective masses of electron (upper panel) and hole (lower panel) for β-fPG subjected to equi-biaxial compressive (−4%) and tensile (2%) strains. The unit of effective masses is the free electron mass. (A colour version of this figure can be viewed online.)

constant derived from the band edge energy changes (obtained from the HSE06 functional) with uniaxial strain. The band edge positions with respect to the vacuum level of α-fPG and β-fPG as a function of uniaxial strains are presented in Fig. 8 (b) and (d) at which the linear fit curves give the DP constants. The obtained DP constants are summarized in Table 3. We found that the DP

Table 3
Calculated effective mass (m_i^*) around band edge positions, deformation potential constant ($E_{d,i}$), and mobility (μ_i) of electron and hole for α-fPG and β-fPG at $T = 300$ K.

Structure	Charge carrier	m_x^*/m_0	m_y^*/m_0	$E_{d,x}$ (eV)	$E_{d,y}$ (eV)	μ_x (Eq. (4)) ($cm^2\ V^{-1}s^{-1}$)	μ_y (Eq. (4)) ($cm^2\ V^{-1}s^{-1}$)	μ_x (Eq. (5)) ($cm^2\ V^{-1}s^{-1}$)	μ_y (Eq. (5)) ($cm^2\ V^{-1}s^{-1}$)
α-fPG	electron	0.17	0.17	9.42	9.42	0.17×10^4	0.17×10^4	0.17×10^4	0.17×10^4
	hole	0.16	0.16	1.68	1.68	6.50×10^4	6.50×10^4	6.50×10^4	6.50×10^4
β-fPG	electron	0.23	0.31	6.21	8.97	0.17×10^4	0.05×10^4	0.16×10^4	0.06×10^4
	hole	0.14	0.19	3.20	1.21	1.64×10^4	7.39×10^4	1.57×10^4	7.74×10^4

constants for electrons are much larger than those for holes. This is related to the carrier-acoustic phonon interaction. In other words, the DP constant is a feature of the coupling strength of the electron (or hole) to the acoustic phonon [41]. A weaker electron (or hole)-acoustic-phonon interaction results in a smaller DP constant value. Our results indicated that the electrons in α-fPG and β-fPG are more strongly scattered by the acoustic phonon than the hole. Having the analysis of the effective mass, in-plane stiffness constant, and DP constant, we calculated the charge carrier mobility along the *i* transport direction at 300 K using Eq. 4. For α-fPG, the calculated electron mobility in the *x* direction is $0.17 \times 10^4\ cm^2V^{-1}s^{-1}$ (which should be the same in the *y*-direction due to the structure geometry). Moreover, the hole mobility in the *x*-direction is calculated as $6.50 \times 10^4\ cm^2V^{-1}s^{-1}$, which is ~38 times higher than that of electron due to the large difference in the DP constant. We noted that the DP constant takes a quadratic term in the denominator of Eq. 4 and has a higher-order effect than other terms (the effective mass and elastic stiffness constant) on the carrier mobility. The high carrier mobility of α-fPG would endow it with many important applications such as the separation of electrons and holes. For β-fPG, the carrier mobility of electron in the *x* and *y* direction is found to be 0.17×10^4 and $0.05 \times 10^4\ cm^2V^{-1}s^{-1}$ while 1.64×10^4 and $7.39 \times 10^4\ cm^2V^{-1}s^{-1}$ for the hole, respectively. The hole mobility of the β-fPG, as well as α-fPG, is higher than that of tetrahexcarbon ($440\ cm^2V^{-1}s^{-1}$) [42] and MoS_2 ($270\ cm^2V^{-1}s^{-1}$) [43]. Hence, the mobility of β-fPG is highly dependent on the carrier type and transport direction. The high and anisotropic carrier mobility make β-fPG a promising candidate for future electronics.

Concerning the great anisotropy in the DP constants, a new formula for the acoustic phonon-limited mobility in anisotropic 2D semiconductors was given by Lang et al. [44] as follows;

$$\mu_i = \frac{e\hbar^3\left(\frac{5C_i+3C_j}{8}\right)}{k_B T (m_i^*)^{3/2}(m_j^*)^{1/2}\left(\frac{9E_{d,i}^2+7E_{d,i}E_{d,j}+4E_{d,j}^2}{20}\right)} \quad (5)$$

where the carrier mobility depends on carrier effective mass, elastic stiffness constant, and DP constant, not only along the longitudinal charge transport direction but also along the in-plane transverse direction. In other words, it is not neglected the scattering from the *x*-direction when considering the carrier mobility along the *y*-direction. Thus, for anisotropic materials, Eq. 5 is a significant improvement to Eq. 4. The calculated charge carrier mobility values using Eq. (5) are summarized in Table 3.

3.4. Optical properties

We further analyzed the optical properties of the fPG monolayers. Deduced from the frequency-dependent complex dielectric function (given as $\epsilon(\omega) = \epsilon_1(\omega) + i\epsilon_2(\omega)$), we calculated the optical absorption coefficient $\alpha(\omega)$ using the following equation [45],

$$\alpha(\omega) = \sqrt{2}\omega\left(\sqrt{\epsilon_1^2(\omega) + \epsilon_2^2(\omega)} - \epsilon_1(\omega)\right)^{1/2} \quad (6)$$

where $\epsilon_1(\omega)$ and $\epsilon_2(\omega)$ are the real and imaginary parts of the dielectric constants, respectively. Considering the strong quantum confinement effects and small Coulomb screening in 2D materials, we focus on many-body effects including electron-electron and electron-hole interactions, which are out of the framework of ordinary DFT methods. It is known that the many-body interactions accurately describe the optical properties of 2D materials and could produce results in good agreement with experiments [46]. A typical way to include the many-body effects is GW approximation [26]. We thus computed the dielectric constants by adopting the GW method. We calculated the quasi-particle (QP) energies in the single-shot GW approximation (GW_0). By employing GW_0, we obtained the quasi-particle band gap (fundamental gap) of α-fPG and β-fPG as 1.92 eV and 0.91 eV respectively, which are higher than those from the HSE functional. It is worth noting that, in our calculations, the DFT band gap values obtained from the HSE06 functional were notably larger than those from the PBE calculations, but were significantly lower than the band gaps from all the GW calculations.

Employing the GW_0 method performed within the random phase approximation (GW_0+RPA), including electron-electron correlations and neglecting electron-hole interactions, we computed the optical absorption spectra of the α-fPG and β-fPG monolayers. Considering the electron-hole interaction as well as electron-electron interaction, we next computed the photo-excited states and optical absorption spectra by adopting GW_0+BSE approximations [47]. Fig. 10 shows the optical absorption spectrum of α-fPG and β-fPG with polarization vectors parallel to their in-plane using the GW_0-RPA and GW_0-BSE methods. It can be seen that when including the electron-hole coupling in the GW_0 calculations, the optical absorption spectrum is changed dramatically. From Fig. 10, the GW_0+BSE optical spectrum of α-fPG and β-fPG displays a global shift towards lower energies as compared to the GW_0+RPA optical spectrum. It can be seen that α-fPG monolayer has substantially large absorption in the range of 1.8–5 eV, in which prominent peaks can be observed. The first absorption peaks in α-fGP and β-fPG, which are below the QP band gap and ascribed to the excitonic peaks, are utterly missing in the GW_0+RPA spectrum. These excitonic peaks are evidence of the quantum confinement effects in the 2D fPG semiconductors. Importantly, α-fPG can significantly absorb the visible light as well as the ultraviolet (UV) light while β-fPG monolayer is seen to possess a high optical response with anisotropy in a very broad spectral region ranging from near-infrared to UV. This anisotropy in β-fPG stems from the intrinsic anisotropy of the atomic structure. Remarkably, the optical absorption coefficient of α-fPG and β-fPG can reach $10^5\ cm^{-1}$, which is comparable to that of organic perovskite solar cells [48]. Therefore, all these remarkable optical properties enable the fPG semiconductors to be promising candidates for use in optoelectronic devices.

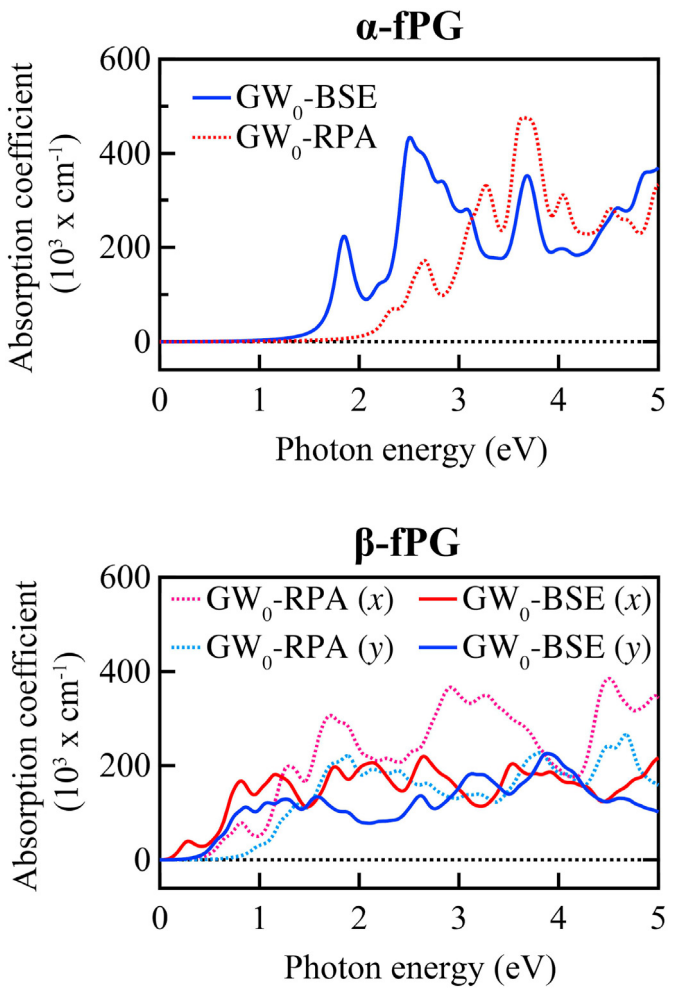

Fig. 10. Variation of optical absorption coefficient with respect to the photon energy for α-fPG and β-fPG by employing GW_0+RPA and GW_0+BSE methods, which are depicted in dashed and solid lines, respectively. (A colour version of this figure can be viewed online.)

4. Conclusions

In summary, we theoretically introduce a new family of 2D carbon allotropes, abbreviated as four-penta-graphenes (fPG). We have found that the fPG monolayers are energetically more favorable than pentagraphene and the experimentally synthesized graphdiyne allotropes. The dynamical stability of the fPG monolayers is confirmed by the absence of imaginary frequency of the phonon modes in the calculated phonon dispersion curves. They can withstand temperatures as high as 1000 K, verifying their thermal stability. The obtained elastic stiffness constants meet the criteria for the mechanical stability. In addition to the robust stability, the fPG monolayers exhibit remarkable mechanical, electronic, and optical properties. We have demonstrated that α-fPG has isotropic Young's modulus and Poisson's ratio whereas β-fPG and γ-fPG exhibit highly anisotropic mechcanical behavior. Moreover, the fPG monolayers are auxetic materials with near zero PR. Remarkably, the sign of PR can be effectively changed from negative to positive or positive to negative by strain engineering. According to the electronic band structure calculations, α-fPG and β-fPG are intrinsic semiconductors with band gap of 1.06 eV and 0.43 eV, respectively while γ-fPG is metallic. We have shown that the sp^2/sp^3 and $sp/sp^2/sp^3$ ratio of carbon atoms in the fPG monolayers is of significant importance in the electronic properties. For instance, the insertion of acetylenic groups in between the fP units results in reducing the band gap energy. The electronic band gap and band edge positions for α-fPG and β-fPG can be tailored by strain engineering. Importantly, both undergo a transition from indirect to direct band gap semiconductor under compressive strain and semiconductor-to-metal under tensile strain applications. The effective mass of hole and electron indicates the strong anisotropic transport behavior and is improved by strain engineering. According to the optical calculations, we clearly examine the excitonic peaks in the optical spectra of the fPG semiconductors by including electron-hole interactions. Our results highlight the unique mechanical, electronic, and optical properties in the 2D carbon allotropes, which are expected to be potential candidates for nanoelectronics and optoelectronics.

CRediT authorship contribution statement

Mehmet Emin Kilic: Conceptualization, Investigation, Writing – original draft, Writing – review & editing, Visualization. **Kwang-Ryeol Lee:** Writing – review & editing, Supervision.

Declaration of competing interest

The authors declare that they have no known competing financial interests or personal relationships that could have appeared to influence the work reported in this paper.

Acknowledgement

This work was supported by the Brain Pool Program funded by the Ministry of Science and ICT through the National Research Foundation of Korea (2020H1D3A1A02081517).

Appendix A. Supplementary data

Supplementary data to this article can be found online at https://doi.org/10.1016/j.carbon.2022.04.018.

References

[1] K.S. Novoselov, A.K. Geim, S.V. Morozov, D. Jiang, Y. Zhang, S.V. Dubonos, I.V. Grigorieva, A.A. Firsov, Electric field effect in atomically thin carbon films, Science 306 (5696) (2004) 666–669.
[2] K.S. Novoselov, A.K. Geim, S.V. Morozov, D. Jiang, M.I. Katsnelson, I. Grigorieva, S. Dubonos, Firsov, Two-dimensional gas of massless Dirac fermions in graphene, Nature 438 (7065) (2005) 197–200.
[3] C. Lee, X. Wei, J.W. Kysar, J. Hone, Measurement of the elastic properties and intrinsic strength of monolayer graphene, Science 321 (5887) (2008) 385–388.
[4] W. Choi, I. Lahiri, R. Seelaboyina, Y.S. Kang, Synthesis of graphene and its applications: a review, Crit. Rev. Solid State Mater. Sci. 35 (1) (2010) 52–71.
[5] R. Baughman, H. Eckhardt, M. Kertesz, Structure-property predictions for new planar forms of carbon: layered phases containing sp 2 and sp atoms, J. Chem. Phys. 87 (11) (1987) 6687–6699.
[6] G. Li, Y. Li, H. Liu, Y. Guo, Y. Li, D. Zhu, Architecture of graphdiyne nanoscale films, ChemComm 46 (19) (2010) 3256–3258.
[7] H. Lu, S.-D. Li, Two-dimensional carbon allotropes from graphene to graphyne, J. Math. Chem. C 1 (23) (2013) 3677–3680.
[8] X. Gao, H. Liu, D. Wang, J. Zhang, Graphdiyne: synthesis, properties, and applications, Chem. Soc. Rev. 48 (3) (2019) 908–936.
[9] Z. Wang, X.-F. Zhou, X. Zhang, Q. Zhu, H. Dong, M. Zhao, A.R. Oganov, Phagraphene: a low-energy graphene allotrope composed of 5–6–7 carbon rings with distorted Dirac cones, Nano Lett. 15 (9) (2015) 6182–6186.
[10] H. Prinzbach, A. Weiler, P. Landenberger, F. Wahl, J. Wörth, L.T. Scott, M. Gelmont, D. Olevano, B.v. Issendorff, Gas-phase production and photoelectron spectroscopy of the smallest fullerene, C 20, Nature 407 (6800) (2000) 60–63.
[11] J.I. Cerdá, J. Sławińska, G. Le Lay, A.C. Marele, J.M. Gómez-Rodríguez, M.E. Dávila, Unveiling the pentagonal nature of perfectly aligned single-and double-strand Si nano-ribbons on Ag (110), Nat. Commun. 7 (1) (2016) 1–7.
[12] A.D. Oyedele, S. Yang, L. Liang, A.A. Puretzky, K. Wang, J. Zhang, P. Yu, P.R. Pudasaini, A.W. Ghosh, Z. Liu, PdSe2: pentagonal two-dimensional layers

with high air stability for electronics, J. Am. Chem. Soc. 139 (40) (2017) 14090–14097.
[13] Q. Liang, Q. Wang, Q. Zhang, J. Wei, S.X. Lim, R. Zhu, J. Hu, W. Wei, C. Lee, C. Sow, et al., High-performance, room temperature, ultra-broadband photodetectors based on air-stable $PdSe_2$, Adv. Mater. 31 (24) (2019), 1807609.
[14] S. Zhang, J. Zhou, Q. Wang, X. Chen, Y. Kawazoe, P. Jena, Penta-graphene: a new carbon allotrope, Proc. Natl. Acad. Sci. Unit. States Am. 112 (8) (2015) 2372–2377.
[15] T. Zhang, Y. Ma, B. Huang, Y. Dai, Two-dimensional penta-BN2 with high specific capacity for Li-ion batteries, ACS Appl. Mater. Interfaces 11 (6) (2019) 6104–6110.
[16] M.E. Kilic, K.-R. Lee, Penta carbides: two-dimensional group-IV semiconductors containing C2 dimers for nanoelectronics and photocatalytic water splitting, Phys. Rev. Mat. 5 (6) (2021), 065404.
[17] M.E. Kilic, K.-R. Lee, Novel two-dimensional group-IV carbides containing C2 dimers: sizable direct band gap, high carrier mobility, and anisotropic properties for nanoelectronics, Carbon 181 (2021) 421–432.
[18] P.V. Silva, M. Fadel, A.G. Souza Filho, V. Meunier, E.C. Girao, Tripentaphenes: two-dimensional acepentalene-based nanocarbon allotropes, Phys. Chem. Chem. Phys. 22 (40) (2020) 23195–23206.
[19] Z. Zhuo, X. Wu, J. Yang, Me-graphene: a graphene allotrope with near zero Poisson's ratio, sizeable band gap, and high carrier mobility, Nanoscale 12 (37) (2020) 19359–19366.
[20] B. Ram, H. Mizuseki, C568: a new two-dimensional sp2-sp3 hybridized allotrope of carbon, Carbon 158 (2020) 827–835.
[21] B.R. Venepalli, W.C. Agosta, Fenestranes and the flattening of tetrahedral carbon, Chem. Rev. 87 (2) (1987) 399–410.
[22] G. Kresse, J. Furthmüller, Efficiency of ab-initio total energy calculations for metals and semiconductors using a plane-wave basis set, Comput. Mater. Sci. 6 (1) (1996) 15–50.
[23] P.E. Blöchl, Projector augmented-wave method, Phys. Rev. B 50 (24) (1994), 17953.
[24] J.P. Perdew, K. Burke, M. Ernzerhof, Generalized gradient approximation made simple, Phys. Rev. Lett. 77 (18) (1996) 3865.
[25] J. Heyd, G.E. Scuseria, M. Ernzerhof, Hybrid functionals based on a screened coulomb potential, J. Chem. Phys. 118 (18) (2003) 8207–8215.
[26] G. Onida, L. Reining, A. Rubio, Electronic excitations: density-functional versus many-body green's-function approaches, Rev. Mod. Phys. 74 (2) (2002) 601.
[27] A. Togo, I. Tanaka, First principles phonon calculations in materials science, Scripta Mater. 108 (2015) 1–5.
[28] S. Nosé, A unified formulation of the constant temperature molecular dynamics methods, J. Chem. Phys. 81 (1) (1984) 511–519.
[29] E. Cadelano, P.L. Palla, S. Giordano, L. Colombo, Elastic properties of hydrogenated graphene, Phys. Rev. B 82 (23) (2010), 235414.
[30] P. Yan, T. Ouyang, C. He, J. Li, C. Zhang, C. Tang, J. Zhong, Newly discovered graphyne allotrope with rare and robust Dirac node loop, Nanoscale 13 (6) (2021) 3564–3571.
[31] B.G. Kim, H.J. Choi, Graphyne: hexagonal network of carbon with versatile Dirac cones, Phys. Rev. B 86 (11) (2012), 115435.
[32] Y. Li, L. Xu, H. Liu, Y. Li, Graphdiyne and graphyne: from theoretical predictions to practical construction, Chem. Soc. Rev. 43 (8) (2014) 2572–2586.
[33] N. Narita, S. Nagai, S. Suzuki, K. Nakao, Optimized geometries and electronic structures of graphyne and its family, Phys. Rev. B 58 (16) (1998), 11009.
[34] M. Born, K. Huang, Dynamical Theory of Crystal Lattices, Oxford, 1954.
[35] M.E. Kilic, K.-R. Lee, Tuning the electronic, mechanical, thermal, and optical properties of tetrahexcarbon via hydrogenation, Carbon 161 (2020) 71–82.
[36] S.K. Georgantzinos, S.G. Siampanis, Size-dependent elastic mechanical properties of γ-graphyne structures: a comprehensive finite element investigation, Mater. Des. 202 (2021), 109524.
[37] M.E. Kilic, K.-R. Lee, Novel two-dimensional tetrahexagonal boron nitride with a sizable band gap and a sign-tunable Poisson's ratio, Nanoscale 13 (20) (2021) 9303–9314.
[38] M.E. Kilic, K.-R. Lee, First-principles study of fluorinated tetrahexcarbon: stable configurations, thermal, mechanical, and electronic properties, J. Phys. Chem. C 124 (15) (2020) 8225–8235.
[39] M.E. Kilic, K.-R. Lee, Auxetic, flexible, and strain-tunable two-dimensional th-AlN for photocatalytic visible light water splitting with anisotropic high carrier mobility, J. Mater. Chem. C 9 (14) (2021) 4971–4977.
[40] J. Bardeen, W. Shockley, Deformation potentials and mobilities in non-polar crystals, Phys. Rev. 80 (1) (1950) 72.
[41] M. Long, L. Tang, D. Wang, Y. Li, Z. Shuai, Electronic structure and carrier mobility in graphdiyne sheet and nanoribbons: theoretical predictions, ACS Nano 5 (4) (2011) 2593–2600.
[42] M.E. Kilic, K.-R. Lee, Tetrahex carbides: two-dimensional group-IV materials for nanoelectronics and photocatalytic water splitting, Carbon 174 (2021) 368–381.
[43] Z. Jin, X. Li, J.T. Mullen, K.W. Kim, Intrinsic transport properties of electrons and holes in monolayer transition-metal dichalcogenides, Phys. Rev. B 90 (4) (2014), 045422.
[44] H. Lang, S. Zhang, Z. Liu, Mobility anisotropy of two-dimensional semiconductors, Phys. Rev. B 94 (23) (2016), 235306.
[45] S. Saha, T. Sinha, A. Mookerjee, Electronic structure, chemical bonding, and optical properties of paraelectric BaTiO3, Phys. Rev. B 62 (13) (2000) 8828.
[46] A. Marini, R. Del Sole, Dynamical excitonic effects in metals and semiconductors, Phys. Rev. Lett. 91 (17) (2003), 176402.
[47] E.E. Salpeter, H.A. Bethe, A relativistic equation for bound-state problems, Phys. Rev. 84 (6) (1951) 1232.
[48] N.J. Jeon, J.H. Noh, Y.C. Kim, W.S. Yang, S. Ryu, S.I. Seok, Solvent engineering for high-performance inorganic–organic hybrid perovskite solar cells, Nat. Mater. 13 (9) (2014) 897–903.